Chemical Science

ROYAL SOCIETY OF CHEMISTRY

EDGE ARTICLE

View Article Online
View Journal | View Issue

Cite this: *Chem. Sci.*, 2025, **16**, 14668

All publication charges for this article have been paid for by the Royal Society of Chemistry

Mimicking NADPH oxidase and lipoxygenase by using a biodegradable single-site catalyst *via* a cascade reaction to trigger tumor-specific ferroptosis†

Xiyang Ge,[a] Yiyan Yin,[a] Xiaoni Wang,[a] Xiang Li,[ab] Jin Ouyang [c] and Na Na *[a]

Ferroptosis exhibits promising potential in cancer therapy *via* lipid peroxidation (LPO) accumulation, while its therapeutic efficacy is normally limited by inadequate ROS production and adverse effects on normal tissues. Here, a TME-activated *in situ* synthesis of a single-site catalyst (Fe(II)–PW_{11}) is reported, which triggers ferroptosis by mimicking natural enzyme activities of NADPH oxidase (NOX) and lipoxygenase (LOX) *via* cascade reactions. Upon degradation of the nanocarrier by the overexpressed GSH in an acidic TME, Fe(II)–PW_{11} is obtained through the coordination of Fe^{2+} into lacunary phosphotungstic acid (PW_{11}). Subsequently, Fe(II)–PW_{11} catalyzes NADPH depletion and $O_2^{\bullet-}$ generation through a NOX-like process. This facilitates the formation of high-valent Fe(IV)=O–PW_{11}, initiating cascade reactions to generate lipid radicals through hydrogen atom transfer based on LOX-like activity. Thus, Fe(II)–PW_{11} synergistically accelerates LPO accumulation and antioxidant inhibitions, effectively inducing ferroptosis for cancer therapy. Notably, Fe(II)–PW_{11} is degraded into low-toxic debris in normal organs, reducing side effects after treatment. Significantly, the whole process is well confirmed by comprehensive characterization studies including online monitoring *via* ambient mass spectrometry. This work not only reveals a novel ferroptosis-based cancer treatment in a ROS-independent pathway, but also provides a safe therapeutic modality with low toxicity to normal tissues.

Received 3rd April 2025
Accepted 3rd July 2025

DOI: 10.1039/d5sc02512e

rsc.li/chemical-science

Introduction

Ferroptosis is a unique non-apoptotic-regulated cell death, characterized by lipid peroxidation (LPO) accumulation.[1–3] Compared to classical chemotherapeutics, ferroptosis can overcome the high propensities of drug resistance and poor therapeutic efficiencies, exhibiting promising potential in treating therapy-resistant tumors.[4] Recently, nano-materials have been developed for catalyzing ROS generation to induce ferroptosis, for example, converting H_2O_2 to highly active $^{\bullet}OH$ *via* the Fenton reaction.[5,6] However, ROS can be easily deactivated due to their short lifetime and diffusion distance (only about 1 ns and 100 nm)[7] or be depleted by reductants such as glutathione (GSH).[8,9] Although ferroptosis can be enhanced by *in situ* H_2O_2 generation and increasing intracellular iron content, the efficacy of ROS-mediated ferroptosis is still limited by hypoxia and overexpression of various REDOX substances in the tumor microenvironment (TME). Therefore, it would be desirable to develop therapeutic agents that induce ferroptosis through a ROS-independent pathway.

Natural enzymes such as lipoxygenases (LOXs) and NADPH oxidase (NOX) can facilitate LPO accumulation through enzymatic processes.[10,11] As a key enzyme to initiate LPO, LOXs is a non-heme iron-dependent dioxygenase for targeted oxidizing polyunsaturated fatty acid-containing phospholipids (PUFA-PLs).[12,13] As another inducer, NOX could oxidize NADPH into $NADP^+$ along with superoxide radical ($O_2^{\bullet-}$) formation, which inhibits ferroptosis suppression systems.[14–16] Therefore, the synergistic mimicking of both natural enzyme activities could be an ideal strategy for effectively inducing ferroptosis-based antitumor therapy. However, there is still a shortage of reports on ferroptosis induced by mimics with both enzymatic activities, which could be challenged by obscure catalytic mechanisms and achieving synergistic activities in cancer cells.

Besides, some challenges still remain in tumor-specific therapy despite the distinct advantages of ferroptosis-based therapy. For instance, the drug's random distribution during the delivery would cause off-target toxicity to normal tissues. In addition, the postoperative side effects of ferroptosis can also

[a]*Key Laboratory of Radiopharmaceuticals, College of Chemistry, Beijing Normal University, Beijing 100875, China. E-mail: nana@bnu.edu.cn*

[b]*State Key Laboratory for Quality Ensurance and Sustainable Use of Dao-di Herbs, National Resource Center for Chinese Materia Medica, China Academy of Chinese Medical Sciences, Beijing 100700, China*

[c]*Department of Chemistry, Faculty of Arts and Sciences, Beijing Normal University, Zhuhai 519087, China*

† Electronic supplementary information (ESI) available. See DOI: https://doi.org/10.1039/d5sc02512e

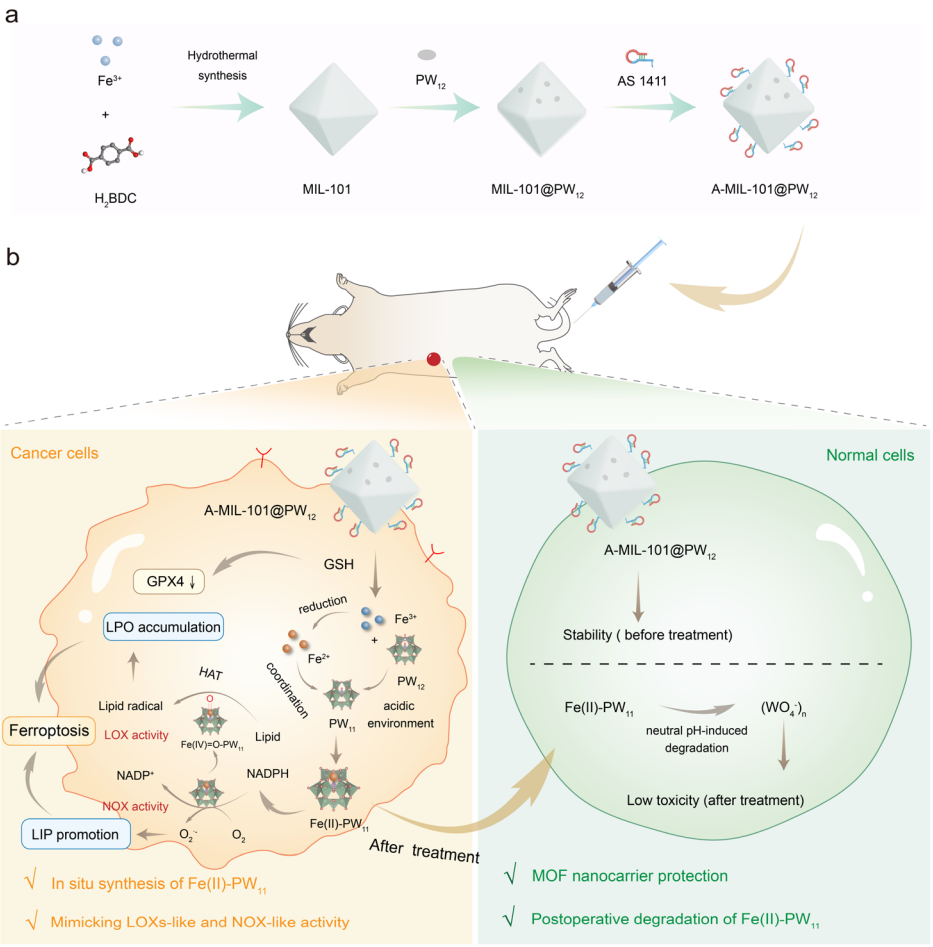

Scheme 1 Illustration of *in situ* synthesis of Fe(II)–PW_{11} for cancer therapy. (a) Preparation of nanocarriers. (b) Ferroptosis induced by the *in situ* synthesized Fe(II)–PW_{11} through mimicking cascade NOX and LOX activities by cascade reactions (in cancer cells) and the postoperative degradation of Fe(II)–PW_{11} (in normal cells).

lead to serious adverse reactions and damage to normal organs, such as kidney damage and neurodegeneration.[17,18] To overcome this limitation, the *in situ* construction of a ferroptosis-inducing catalyst can be a promising strategy in precise cancer therapy.[19,20] However, the complex TME would interfere with the catalyst release and decrease the therapeutic efficiency.[21] Moreover, compared with conventional nanoparticles, the single-site catalysts showed great potential in efficient therapy due to their high atomic utilization of isolated catalytic centers with well-defined geometric and electronic structures.[22,23] Therefore, developing a therapeutic single-site catalyst for the specific activation of ferroptosis is desirable.

Herein, a TME-activated *in situ* synthesis of a single-site catalyst (Fe(II)–PW_{11}) is reported to trigger ferroptosis by mimicking NOX and LOX activity *via* a cascade reaction. As shown in Scheme 1, a nanocarrier A-MIL-101@PW_{12} was constructed by loading phosphotungstic acid (PW_{12}) into iron-based MIL-101 and modified with the AS1411 aptamer. This nanocarrier can target cancer cells and prevent the leaking of PW_{12}. Responding to the TME, Fe^{2+} and lacunary phosphotungstic acid (PW_{11}) were released based on the reduction of A-MIL-101@PW_{12} by GSH and the spontaneous transformation of PW_{12} into PW_{11} under acidic conditions. Thereby, the single-site catalyst of Fe(II)–PW_{11} was *in situ* synthesized through the coordination of Fe^{2+} into PW_{11}. The Fe(II)–PW_{11} presented NOX-like activity to convert NADPH into $NADP^+$ and catalyzed $O_2^{\bullet-}$ generation. This process facilitated the formation of the Fe(IV)=O–PW_{11} intermediate, which subsequently abstracted a hydrogen atom from lipids to generate lipid radicals based on LOX-like activity. The produced $O_2^{\bullet-}$ reacts with intracellular Fe^{3+} and catalyzes the conversion of Fe^{3+} to Fe^{2+} to promote the intracellular labile iron pool (LIP), synergetically triggering LPO. In addition, the GSH consumption-induced GPX-4 deactivation and NADPH depletion severely inhibited ferroptosis suppression systems. Notably, Fe(II)–PW_{11} was degraded into low-toxic WO_4^- in normal tissues. Both *in vivo* and *in vitro* experiments verified that Fe(II)–PW_{11}-induced ferroptosis exhibited potent anticancer efficacy with minimal side effects.

Results and discussion

Preparation and characterization of nanocarriers

The nanocarrier of A-MIL-101@PW_{12} was prepared by a series of procedures (Scheme 1a). First, the iron-based metal–organic

framework MIL-101 was synthesized *via* the solvothermal method using Fe^{3+} and terephthalic acid as additives. Then, PW_{12} was loaded into MIL-101 with a porosity of 2.9–3.4 nm (Fig. 1a).[24] The obtained MIL-101@PW_{12} was washed several times to remove surface-absorbed PW_{12}. As characterized by transmission electron microscopy (TEM), both MIL-101 and MIL-101@PW_{12} exhibited octahedral morphologies (Fig. 1b(i), (ii) and S1†), indicating that the encapsulation did not affect the MIL-101 structure. Meanwhile, small aggregates in MIL-101@PW_{12} represented the loaded PW_{12}. Besides, X-ray diffraction (XRD) peaks of MIL-101 shifted from 5.2° and 5.8° to 5.8° and 6.5° after encapsulation, indicating that the entry of PW_{12} affected the crystal face of MIL-101 (Fig. 1c). Therefore, PW_{12} was confirmed to be successfully loaded onto MIL-101 with a high encapsulation rate of 65.89% (Fig. S2†). To achieve enrichment in the tumor, the AS1411 aptamer was modified onto MIL-101@PW_{12} to form A-MIL-101@PW_{12} through electrostatic interaction, which also showed an octahedral morphology (Fig. 1b(iii)). The energy-dispersive spectroscopy (EDS) mapping demonstrated the uniform distribution of C, O, N, W, P, and Fe elements in A-MIL-101@PW_{12}, confirming its successful preparation.

Moreover, chemical characterization studies were employed to evaluate the construction of A-MIL-101@PW_{12}. By Fourier transform infrared spectroscopy (FT-IR) (Fig. 1d), A-MIL-101@PW_{12} exhibits peaks of proton vibration and C–H vibration at 1693 cm^{-1} and 745 cm^{-1}, C–O stretching vibration at 1389 cm^{-1} and 1569 cm^{-1} and Fe–O stretching vibration at 536 cm^{-1}, attributed to the MIL-101 framework. In addition, the characteristic peaks of PW_{12} (P–O_a at 1076 cm^{-1}, W=O_d at 980 cm^{-1}, W–O_b–W at 889 cm^{-1} and W–O_c–W at 819 cm^{-1}) were also observed in A-MIL-101@PW_{12},[25] which were slightly red-shifted after encapsulation. This indicated that the symmetry of PW_{12} was effectively preserved with no decomposition or structural deformation. In addition, the phosphate stretching vibration of the AS1411 aptamer at 1281 cm^{-1} confirmed the modification of AS1411 onto MIL-101@PW_{12}.[26] This was consistent with the approximately negative zeta potential of A-MIL-101@PW_{12} (Fig. 1e).

The X-ray photoelectron spectroscopy (XPS) analysis verifies the presence of Fe(III) (Fe $2p_{3/2}$ 711.8 and Fe $2p_{1/2}$ 725.3 eV) in A-

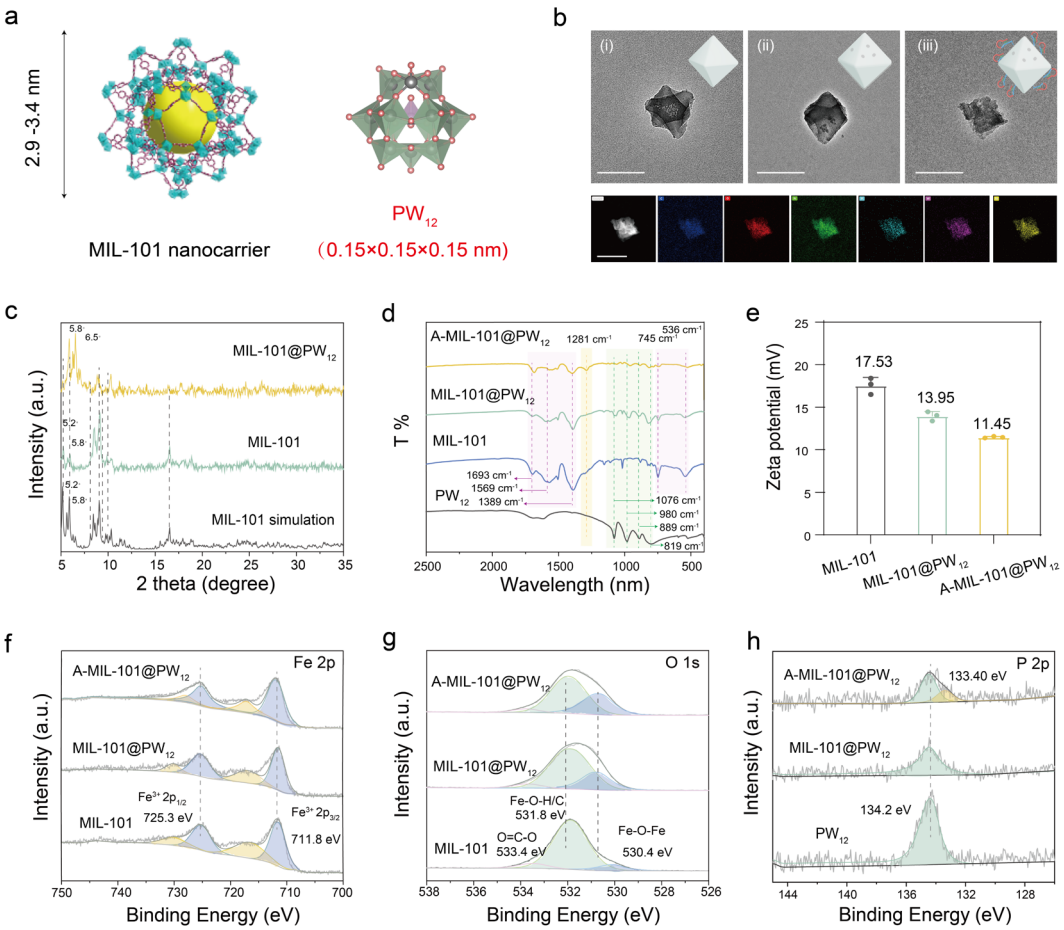

Fig. 1 Characterization of A-MIL-101@PW_{12}. (a) Structure of MIL-101 and PW_{12}. (b) TEM images of MIL-101, MIL-101@PW_{12} and A-MIL-101@PW_{12}, as well as the HADDF image and element mapping of A-MIL-101@PW_{12}. The scale bar is 200 nm. (c) XRD patterns of MIL-101 simulation, MIL-101 and MIL-101@PW_{12}. (d) IR spectra of MIL-101, PW_{12}, MIL-101@PW_{12} and A-MIL-101@PW_{12}. (e) Zeta potential of MIL-101, MIL-101@PW_{12} and A-MIL-101@PW_{12}. (f) Fe 2p XPS and (g) O 1s XPS of MIL-101, MIL-101@PW_{12} and A-MIL-101@PW_{12}. (h) P 2p XPS of PW_{12}, MIL-101@PW_{12} and A-MIL-101@PW_{12}.

MIL-101@PW_{12} (Fig. 1f).[27] In addition, the distinctive peaks of O 1s at Fe–O–Fe (530.4 eV) and Fe–O–H/O–C (531.8 eV) were detected in MIL-101 (Fig. 1g). Upon loading with PW_{12}, these peaks moved to increased binding energy, indicating the interaction between PW_{12} and MIL-101. This was consistent with the shift of the W peaks (Fig. S3†). Furthermore, no obvious change of P 2p at 134.2 eV in A-MIL-101@PW_{12} indicated the structural integrity of PW_{12} (Fig. 1h). Meanwhile, the XPS peak for N 1s (400.9 eV) and P 2 s (133.40 eV) of the AS1411 aptamer demonstrated the successful modification of AS1411 (Fig. S4†). Therefore, A-MIL-101@PW_{12} was successfully synthesized and exhibits stability for drug delivery.

Examinations of *in situ* synthesis of Fe(II)–PW_{11} in the TME and its biodegradable properties

The TME-activated *in situ* synthesis of Fe(II)–PW_{11} was achieved through the A-MIL-101@PW_{12} degradation (Fig. 2a(i)). Briefly, A-MIL-101@PW_{12} was reduced by GSH to release PW_{12} and Fe^{2+} (eqn (1)). Subsequently, PW_{12} was spontaneously converted into PW_{11} under acidic conditions (eqn (2)). Finally, Fe^{2+} was rapidly coordinated with PW_{11} to obtain Fe(II)–PW_{11} (eqn (3)). Notably, this catalyst with a single active site possesses a uniform coordination structure, being convenient to explore molecular changes by MS detections for investigating therapy mechanisms.

$$\text{A-MIL-101@PW}_{12} + \text{GSH} \rightarrow \text{Fe}^{2+} + \text{PW}_{12} + \text{GSSG} \quad (1)$$

$$\text{PW}_{12} \xrightarrow{\text{acidic conditions}} \text{PW}_{11} \quad (2)$$

$$\text{Fe}^{2+} + \text{PW}_{11} \xrightarrow{\text{rapidly}} \text{Fe(II)}-\text{PW}_{11} \quad (3)$$

Initially, the spontaneous conversion of PW_{12} to PW_{11} was examined using MS analysis. As demonstrated (Fig. 2b(i) and S5†), PW_{12} ($[PW_{12}O_{40} + H]^{2-}$ at m/z 1438.74, calc. 1438.60) was recorded, while it converted to PW_{11} ($[PW_{11}O_{39} + 5H]^{2-}$ at m/z 1341.17, calc. 1341.14) at pH 5.5. In addition, Fe(II)–PW_{11} ([Fe(II)$PW_{11}O_{39}$ + 3H]$^{2-}$ at m/z 1367.97, calc. 1368.10) at pH 5.5 was

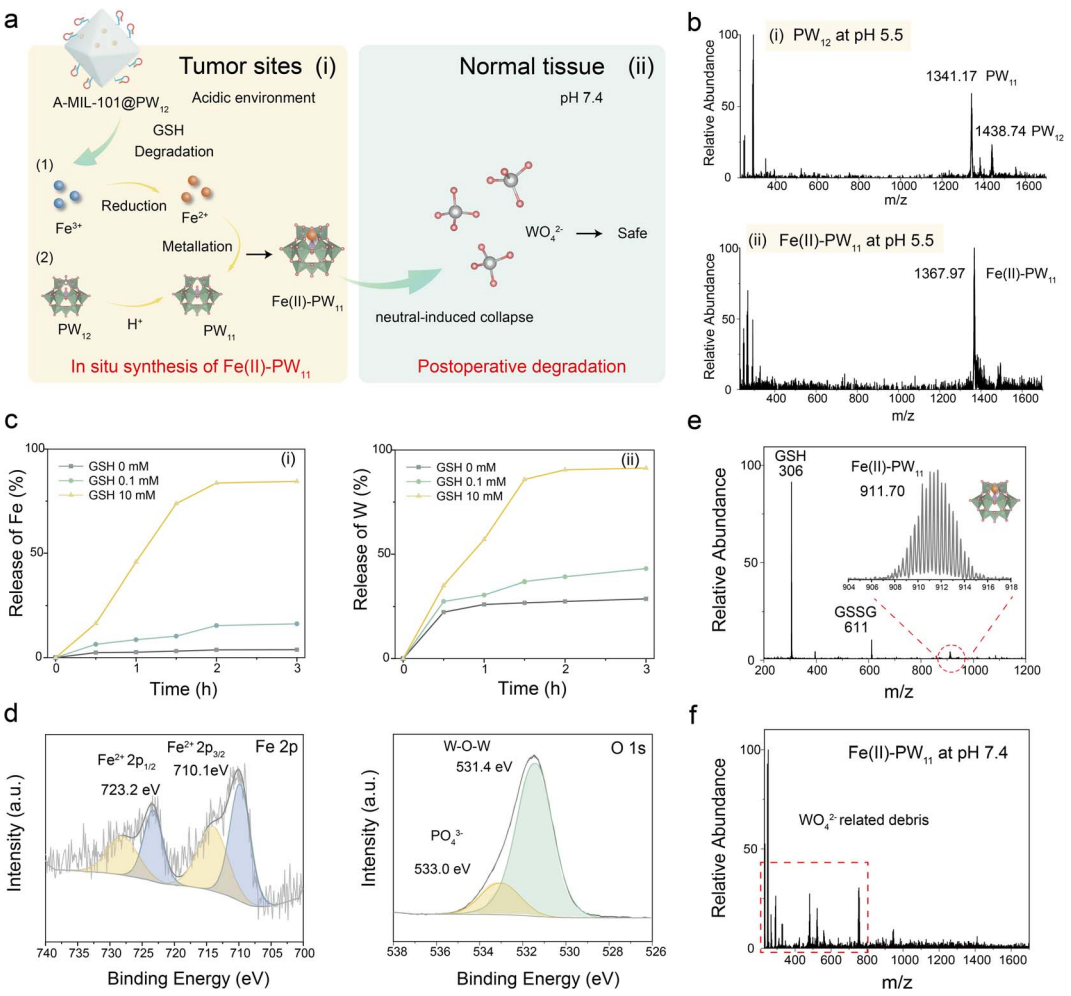

Fig. 2 *In situ* synthesis of Fe(II)–PW_{11}. (a) Scheme of *in situ* synthesis of Fe(II)–PW_{11} at tumor sites and postoperative degradation in normal tissues. (b) The MS spectra of PW_{12} (i) and Fe(II)–PW_{11} at pH 5.5 (ii). (c) Accumulated release profiles of Fe (i) and W (ii) of MIL-101@PW_{12} at different GSH concentrations. (d) XPS peaks of Fe(II)–PW_{11} for Fe and O elements with 10 mM GSH at pH 5.5. (e) The MS spectra of *in situ* synthesized Fe(II)–PW_{11} by mixing A-MIL-101@PW_{12} with 10 mM GSH at pH 5.5. (f) The MS spectra of Fe(II)–PW_{11} at pH 7.4.

also recorded after adding Fe^{2+} into PW_{12} (Fig. 2b(ii)), confirming the coordination of Fe^{2+} to PW_{11}.

Subsequently, to confirm the GSH-induced degradation, the release of Fe^{2+} and PW_{12} was evaluated by inductively coupled plasma (ICP)-MS analysis. As exhibited (Fig. 2c), contents of Fe (i) and W (ii) gradually increased with GSH added and became stable after about 2 h. Meanwhile, the increased UV absorption of Fe^{2+} indicated the reduction of Fe^{3+} by GSH (Fig. S6†). The biodegradability of A-MIL-101@PW_{12} was further confirmed by the structural collapse and the final dissolution of A-MIL-101@PW_{12} after incubating with GSH (Fig. S7†). Besides, XPS confirmed the *in situ* synthesis of Fe(II)–PW_{11} after A-MIL101@PW_{12} degradation (Fig. 2d). As demonstrated, the Fe 2p XPS confirmed the presence of Fe(II) (Fe $2p_{3/2}$ 710.1 eV and Fe $2p_{1/2}$ 723.2 eV), indicating that Fe^{3+} was completely reduced to Fe^{2+} by excess GSH. The O 1s XPS peaks at 531.4 eV and 533.0 eV correspond to the W–O–W and PO_4^{3-} of PW_{11}. This is consistent with the rapid conversion of PW_{12} into PW_{11} under acidic conditions, contributing to the subsequent synthesis of Fe(II)–PW_{11} upon coordination of released Fe^{2+} to PW_{11}.

The *in situ* synthesis of Fe(II)–PW_{11} was further evaluated by MS. As demonstrated by MS characterization (Fig. 2e), the ions of Fe(II)–PW_{11} ($[Fe(II)PW_{11}O_{39} + 2H]^{3-}$ at *m*/*z* 911.70, calc.: 911.73) and the GSH oxidation product ($[GSSG–H]^-$ at *m*/*z* 611) were recorded by mixing A-MIL-101@PW_{12} with GSH at pH 5.5, indicating that Fe(II)–PW_{11} can be synthesized in the TME. While at pH 7.4, no significant signal of Fe(II)–PW_{11} appeared in the A-MIL-101@PW_{12} solution (Fig. S8†). This indicated the stability of A-MIL-101@PW_{12} during delivery. Additionally, this process was monitored with a homemade device of ambient mass spectrometry (Fig. S9†).[28] With GSH added into A-MIL-101@PW_{12}, GSSG and PW_{12} first appeared in 5 min, confirming the efficient degradation of A-MIL-101@PW_{12} by GSH. Thereafter, Fe(II)–PW_{11} gradually increased, which was attributed to the generation of PW_{11} under acidic conditions. In addition, almost no PW_{11} signals were observed due to the rapid coordination of Fe^{2+} with PW_{11}. Therefore, based on the reduction of MIL-101 by GSH and the transformation of PW_{12} into PW_{11} under acidic conditions, Fe(II)–PW_{11} was successfully synthesized in the TME.

Furthermore, the *in situ* synthesized Fe(II)–PW_{11} can be decomposed into low-toxic WO_4^{2-}-related fragments under neutral conditions of normal tissues (Fig. 2a(ii) and eqn (4)). This process avoids the toxicity of Fe(II)–PW_{11} to healthy tissues in postoperative metabolism. To evaluate postoperative degradation, the MS signal of Fe(II)–PW_{11} at pH 7.4 was examined. As demonstrated (Fig. 2f), most debris (at *m*/*z* < 800) was observed, while no signals of Fe(II)–PW_{11} appeared, indicating the disintegration of Fe(II)–PW_{11} in the neutral environment. This was consistent with UV-vis spectra of PW_{12} and Fe(II)–PW_{11} under different conditions (Fig. S10†). Besides, the generation of WO_4^{2-} debris was directly confirmed by the *in situ* Raman spectroscopy characterization (Fig. S11†), showing the increased characteristic bond of WO_4^{2-} (931 cm^{-1}) along with the decrease in Fe(II)–PW_{11} peaks (at 995 and 980 cm^{-1}).[29–31] This neutral environment-induced degradation reduced toxicity to normal tissues, showing potential in selective and efficient therapy.

$$\text{Fe(II)}-\text{PW}_{11} \xrightarrow{\text{neutral conditions}} n\left(\text{WO}_4^{2-}\right) \quad (4)$$

NOX-like activity of Fe(II)–PW_{11}

The *in situ* synthesized Fe(II)–PW_{11} exhibited NOX-like activity by accepting electrons from NADPH, and hence catalyzing the conversion of O_2 to $O_2^{\bullet-}$. First, the NOX-like activity was evaluated by UV-vis spectroscopy analysis. As demonstrated, the absorbance of NADPH decreased at 339 nm after adding Fe(II)–PW_{11} (Fig. 3a), while no significant change in NADPH was observed in the absence of Fe(II)–PW_{11}, indicating that NADPH oxidation was catalyzed by Fe(II)–PW_{11} (Fig. S12†). Besides, the ions of $[NADP–2H]^-$ at *m*/*z* 742 verified the $NADP^+$ generation in the reaction system (Fig. 3b). The electron paramagnetic resonance (EPR) analysis was conducted using 5-(2,2-dimethyl-1,3-propoxycyclo-phosphoryl)-5-methyl-1-pyrroline-*N*-oxide (CYPMPO) as a spin trap. In the presence of CYPMPO, the carbon-centered NADP$^\bullet$ radical was detected in the Fe(II)–PW_{11} and NADPH solution (Fig. 3c).[32] Notably, $O_2^{\bullet-}$ was also observed in the reaction, confirmed by the EPR signal of BMPO–OOH with 5-*tert*-butoxycarbonyl-5-methyl-1-pyrroline *N*-oxide (BMPO) as a trapping agent (Fig. S13†).[33] In addition, H_2O_2 was detected by peroxide detection strips (Fig. S14†), which were formed by the interaction between $O_2^{\bullet-}$ and H^+ along with the electron transfer from the NADP$^\bullet$ radical to $NADP^+$.[34] These results confirmed the superior NOX-like activity of Fe(II)–PW_{11} for catalyzing O_2 into $O_2^{\bullet-}$ and the oxidation of NADPH to $NADP^+$.

Furthermore, the cyclic voltammetry (CV) current of Fe(II)–PW_{11} significantly increased after adding NADPH in air, indicating the occurrence of electron transfer between Fe(II)–PW_{11} and NADPH (Fig. 3d). However, no obvious change in Fe(II)–PW_{11} in the N_2-treated solution demonstrated the importance of O_2 in the Fe(II)–PW_{11} catalysis process. The electron transfer in the reaction between Fe(II)–PW_{11} and NADPH may be facilitated by the coordination of O_2 with Fe. Thereby, the coordination of O_2 by Fe(II)–PW_{11} was investigated through Density Functional Theory (DFT) calculations.[35] As calculated (Fig. 3e), O_2 was connected to an Fe atom in an end-on way, exhibiting a stretched O–O bond (1.24 Å) compared with that in O_2 (1.20 Å). This indicated that Fe(II)–PW_{11} can activate O_2 *via* the Fe–O bond to facilitate the catalytic reaction.

The intermediates in the reaction were evaluated through MS detections. As a result (Fig. 3f), the intermediate of Fe(III)–PW_{11}–O_2^- ($[Fe(III)PW_{11}O_{39}–O_2^- + 3H]^{2-}$ at *m*/*z* 1384.12, calc. 1384.09) was first formed, confirming the ability of Fe(II)–PW_{11} to absorb O_2. After adding NADPH, the intermediate of Fe(II)–PW_{11}–$O_2^{\bullet-}$ ($[Fe(II)PW_{11}O_{39}–O_2^{\bullet-} + 4H]^{2-}$ at *m*/*z* 1384.60, calc. 1384.60) was formed during the reaction, which also confirmed the formation of $O_2^{\bullet-}$. In addition, EPR analysis demonstrated that the high-spin Fe ($S = 2$, $g = 11.58$) in the *in situ* synthesized Fe(II)–PW_{11} was converted to the low-spin state ($S = 1/2$, $g = 2.00$) during O_2 coordination (Fig. 3g). This indicated that the change of Fe spin would facilitate the activation of O_2,

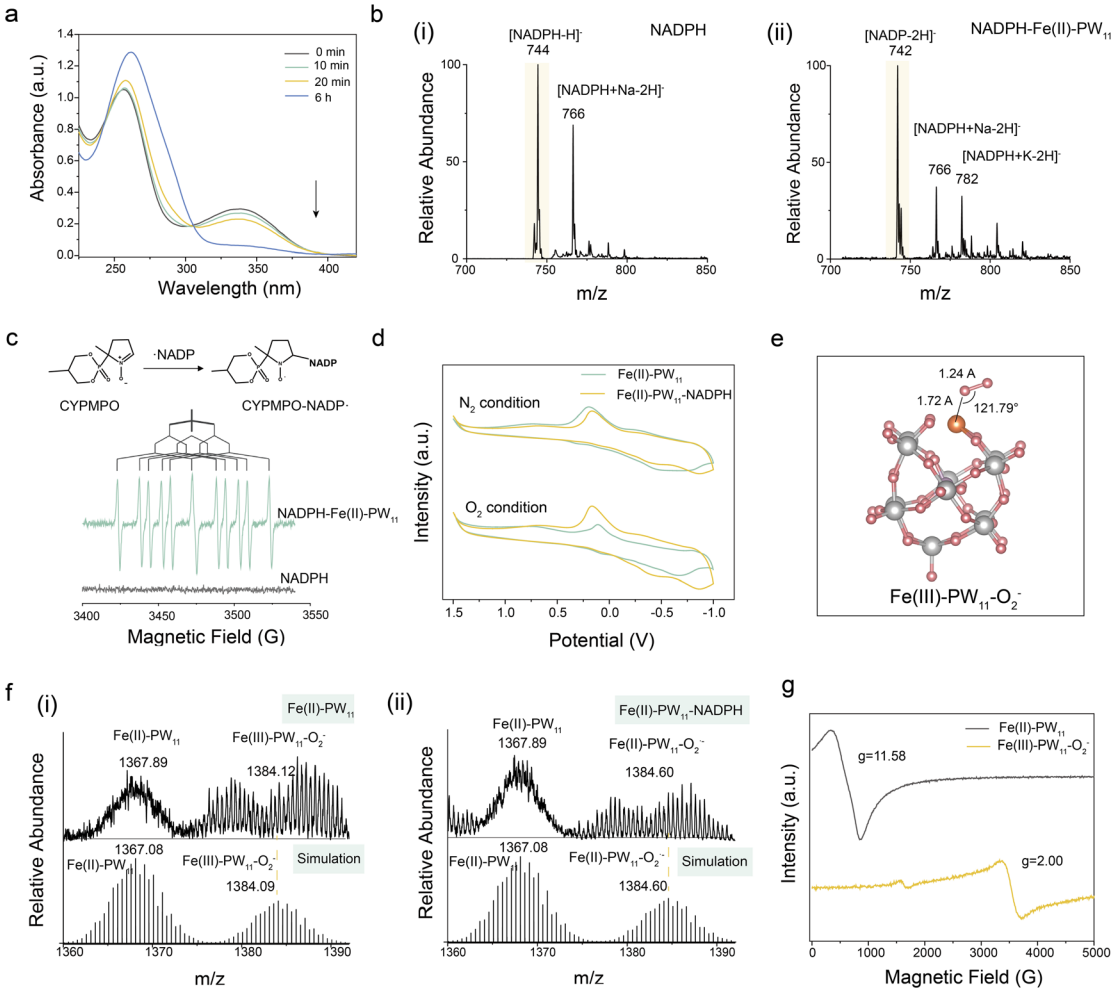

Fig. 3 The NOX-like activity of Fe(II)–PW_{11}. (a) The UV-vis spectra of NADPH after treatment with Fe(II)–PW_{11} in air at different times. (b) Mass spectra of NADPH before (i) and after (ii) adding Fe(II)–PW_{11} in air. (c) EPR spectra of CYPMPO–NADP$^{\bullet}$. c(CYPMPO) = 100 mM. (d) The CV curves of Fe(II)–PW_{11} with or without adding NADPH in air and N_2. (e) The optimization structure of Fe(III)–PW_{11}–O_2^-. (f) Mass spectra of Fe(II)–PW_{11} before (i) and after (ii) adding NADPH in air. (g) EPR spectra of the *in situ* synthesized Fe(II)–PW_{11} before and after absorbing with O_2.

permitting electron transfer from NADPH. To explore the effect of Fe(II)–PW_{11}, the electron properties were calculated using the Multiwfn software package.[36] As demonstrated (Fig. S15†), the LUMO energy of O_2 in Fe(III)–PW_{11}–O_2^- was lower than that of the O_2 empty orbital ($\pi^*_{2p_y}$). This indicated that Fe(II)–PW_{11} can activate O_2 to accept the electron from NADPH easily.

Consequently, the mechanism of NOX-like activity of Fe(II)–PW_{11} was confirmed (Fig. S16†). Initially, Fe(II)–PW_{11} activates O_2 by forming the Fe(III)–PW_{11}–O_2^- intermediate through spin change. With NADPH present, an electron is transferred from NADPH to Fe(III)–PW_{11}–O_2^- to form Fe(II)–PW_{11}–$O_2^{\bullet-}$ and $NADPH^{+\bullet}$, easily forming the NADP$^{\bullet}$ radical upon deprotonation. Finally, an electron was transferred from NADP$^{\bullet}$ to $O_2^{\bullet-}$ that desorbed from Fe(II)–PW_{11}, facilitating the generation of $NADP^+$ and H_2O_2. It should be noted that the present single-site catalyst of Fe(II)–PW_{11} exhibited better NOX-like performance than the conventional catalysts of Fe_3O_4 nanoparticles (the characterization studies are shown in Fig. S17†), demonstrated by the evaluation of NADPH content after treatment with both species (Fig. S18†).

LOX-like activity of Fe(II)–PW_{11}

Natural LOX catalyzes the peroxidation of PUFA through hydrogen atom transfer (HAT) in the presence of an active site of Fe(III) (Fig. 4a). During the catalytic reaction in an Fe(II)–PW_{11} system, the O_2-activated generation of high-valent Fe species can catalyze the LPO process through HAT, enabling cascade NOX-like and LOX-like activities of Fe(II)–PW_{11}. Initially, linoleic acid (LA), a kind of PUFA, was selected as the model for examinations. As a result (Fig. 4b), only $[LA–H]^-$ at m/z 279 was recorded after adding Fe(II)–PW_{11} into LA. While with NADPH added, LA peroxidation was confirmed by recording ions of $[LA–OH–H]^-$ (m/z 295) and $[LA–OOH–H]^-$ (m/z 311) (Fig. 4c). Meanwhile, $[NADP–2H]^-$ (m/z 742) demonstrated the formation of $NADP^+$ in the reaction system, confirming enzymatic catalysis of NADPH and LA oxidation upon the cascade reaction catalyzed by Fe(II)–PW_{11}. As the reaction progressed, various oxidation products and peroxidation products of LA at m/z 309 ($[LA{=}O–OH–H]^-$), 325 ($[LA{=}O–OH–OH–H]^-$) and 327 ($[LA–OH–OOH–H]^-$) were observed at the 20 min reaction, respectively (Fig. S19†). Furthermore, other oxidation products and LPO

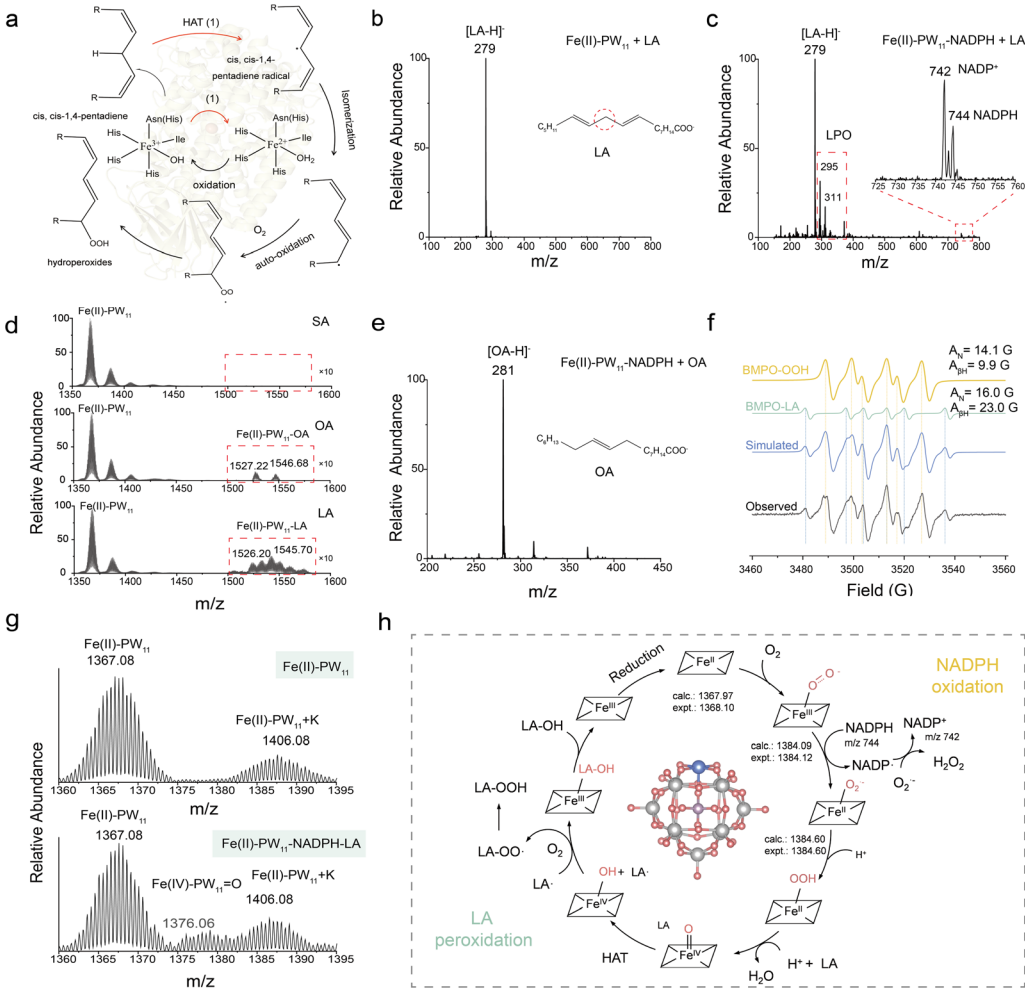

Fig. 4 The LOX-like activity of Fe(II)–PW_{11}. (a) The HAT mechanism of natural LOXs. (b) The MS signal of a mixture of LA and Fe(II)–PW_{11}. (c) The MS signal of LA oxidation and peroxidation products in the Fe(II)–PW_{11}–NADPH system for 5 min. (d) The MS spectra of Fe(II)–PW_{11} with SA, OA and LA added. (e) The MS spectra of the OA–NADPH system with Fe(II)–PW_{11} added. (f) EPR spectra of the LA peroxidation process with BMPO as the trapping agent. (g) The MS spectra of the Fe(IV)–PW_{11}=O intermediate during the reaction. (h) Proposed Fe(II)–PW_{11} catalytic mechanism of enzymatic NOX–LOX-like activities upon cascade reactions.

markers of 4-hydroxynonenal (4-HNE) (*m*/*z* 171 and 155) were detected at 1 h (Fig. S20†), indicating the deep oxidation and bond breakage of LA. The corresponding structures were confirmed by collision-induced dissociation (CID) MS (Fig. S21†).

To confirm the specific peroxidation of PUFA, saturated fatty acids (stearic acid, SA) and monounsaturated fatty acids (oleic acid, OA) were selected as the models. The adsorption of SA, OA and LA on the catalytic site of Fe(II)–PW_{11} was evaluated by mixing Fe(II)–PW_{11} with LA, OA and SA, respectively (Fig. 4d). As result, the ions of $[Fe(II)PW_{11}O_{39}–OA + H_2O + 3H]^{2-}$ (*m*/*z* 1527.22, calc. 1527.19), $[Fe(II)PW_{11}O_{39}–OA–2H_2O + K + 2H]^{2-}$ (*m*/*z* 1546.68, calc. 1546.72), $[Fe(II)PW_{11}O_{39}–LA–H_2O + 3H]^{2-}$ (*m*/*z* 1526.20, calc. 1525.23) and $[Fe(II)PW_{11}O_{39}–LA–2H_2O + K + 2H]^{2-}$ (*m*/*z* 1545.70, calc. 1545.72) were observed, while no signal of Fe(II)–PW_{11}–SA was recorded. This indicated that Fe(II)–PW_{11} could adsorb OA and LA through double bonds for subsequent peroxidation. Furthermore, compared to LA, OA cannot be oxidized in air after adding NADPH (Fig. 4e), further indicating the selective catalytic peroxidation of PUFA by Fe(II)–PW_{11}.

Besides, the peroxidation of PUFA-PLs catalyzed by Fe(II)–PW_{11} was explored. With lecithin (PC) and cuorin (CL) as substrates (the most abundant phospholipids in the body), the peroxidation product ions of $[PC–OOH + H]^+$ (*m*/*z* 790) and $[CL–OOH–2H]^-$ (*m*/*z* 739) were recorded after adding NADPH into the Fe(II)–PW_{11} system (Fig. S22 and S23†). This indicated that the phospholipid chain in cells have no effect on the Fe(II)–PW_{11} catalyzed PUFA-PL peroxidation.

To explore the mechanism of LA peroxidation by Fe(II)–PW_{11}, EPR and MS characterization studies were carried out. In the reaction system (Fig. 4f), the $O_2^{\bullet-}$ and $^{\bullet}$LA radicals were confirmed by the peaks of BMPO–OOH and BMPO–LA, respectively. The signal of BMPO–OOH (A_N and $A_{\beta H}$ at 14.1 G and 9.9 G, respectively) was attributed to $O_2^{\bullet-}$ generation catalyzed by Fe(II)–PW_{11} through NOX-like activity. In addition, the peaks of BMPO–LA (A_N and $A_{\beta H}$ at 16.0 G and 23.0 G) indicated the

formation of the carbon-central ˙LA radical. Notably, the $2A_N + A_{\beta H}$ was calculated to be 55.0 G, attributed to the radical of bisallyllic carbon rather than olefinic carbon (>56 G) and saturated carbon (~52 G). Furthermore, the obvious MS signal of the Fe intermediate of Fe(IV)–PW_{11}=O ($[Fe^{IV}PW_{11}O_{39}{=}O + 3H]^{2-}$ at *m*/*z* 1376.06, calc. 1376.06) was observed after adding NADPH and LA solution (Fig. 4g), which was the most important intermediate in the LPO process. Based on the low-lying unoccupied antibonding orbital, Fe(IV)–PW_{11}=O can easily abstract a hydrogen atom from LA to generate ˙LA, facilitating LA–OO˙ production through autooxidation. In addition, the activation energy of the transient state (TS) of the HAT process was calculated to be 125.5 kcal mol^{-1} with *cis*-2, *cis*-5-heptadiene as a model (Fig. S24†). Therefore, the HAT-based generation of ˙LA was demonstrated, which would support the deduced mechanism of NADPH and LA oxidation upon the cascade reaction.

Consequently, the mechanism of cascade NOX-like and LOX-like activity catalyzed by Fe(II)–PW_{11} can be proposed as shown in Fig. 4h. Initially, Fe(II)–PW_{11} would effectively bind and activate O_2 to form the Fe(III)–PW_{11}–$O_2^{\cdot-}$ intermediate upon the donation of an electron by NADPH. During the oxidation, Fe(II)–PW_{11}–$O_2^{\cdot-}$ is rapidly protonated into an intermediate of Fe(III)–PW_{11}–OOH under acidic conditions. Thereafter, the intermediate of Fe(IV)=O–PW_{11} is formed upon protonation and heterocleavage of the O–O bond, along with losing one water. This intermediate subsequently initiated HAT for ˙LA production. Meanwhile, ˙LA can be oxidized into LAOO˙ radicals in the presence of O_2, promoting the formation of lipid peroxides. The absorbed hydroxyl group can recombine with ˙LA to form Fe(III)–PW_{11}–LA–OH, followed by the release of LA–OH and Fe(III)–PW_{11} unit. Finally, Fe(III)–PW_{11} would accept an electron from NADPH to form Fe(II)–PW_{11}, initiating the next catalytic cycle. It should be noted that the present single-site catalyst of Fe(II)–PW_{11} exhibited better LOX-like performance than the conventional catalysts of Fe_3O_4 nanoparticles, as demonstrated by the monitoring of LA peroxidation by mass spectrometry after treatment with both species (Fig. S25†).

In situ synthesis of Fe(II)–PW_{11} for cancer therapy

As designed, A-MIL-101@PW_{12} can be recognized by receptors of cancer cells for cellular uptake and degraded by upregulated GSH for the *in situ* synthesis of Fe(II)–PW_{11}. Herein, HeLa cells were selected as models to investigate TME-activated *in situ* synthesis. First, the stability of A-MIL-101@PW_{12} was evaluated using hydrodynamic size distributions (DLS) analysis (Fig. S26†), without significant change of the A-MIL-101@PW_{12} size in water, PBS and DMEM cell culture medium at different dispersion times. This indicated that A-MIL-101@PW_{12} exhibited excellent stability under physiological conditions for cancer therapy. To explore the nanomedicine uptake, the fluorescent Cyanine 5 (Cy5) was labeled on the AS1411 aptamer to form Cy5-A-MIL-101@PW_{12} with red fluorescence.[37] As exhibited in both 2D and 3D Z-stack images of HeLa cells (Fig. 5a), the uptake of A-MIL-101@PW_{12} into the cytoplasm was demonstrated by the significantly increased red FL signals. Furthermore, the GSH consumption in HeLa cells was recorded in all groups and much higher consumptions were exhibited in MIL-101@PW_{12} and A-MIL-101@PW_{12} groups (Fig. 5b). This confirmed the GSH-initiated decomposition of MIL-101 nanocarriers and the NADPH-regulated GSH depletion catalyzed by Fe(II)–PW_{11}. Thereafter, *in situ* synthesis of Fe(II)–PW_{11} was confirmed by the detection of Fe(II)–PW_{11} at *m*/*z* 911.75 in the lysate of HeLa cells incubated with A-MIL-101@PW_{12} (Fig. 5c).

To evaluate the therapeutic effect of cancer therapy, the methylthiazole tetrazole (MTT) assay was performed for HeLa cells and HUVECs cultured with different groups. As demonstrated (Fig. 5d), MIL-101, Fe(II)–PW_{11}, MIL-101@PW_{12}, and A-MIL-101@PW_{12} showed hypotoxicity to HUVEC cells, indicating the good biocompatibility of these nanomedicines. Notably, Fe(II)–PW_{11} exhibited high toxicity to HeLa cells but low toxicity to HUVECs, attributed to the degradation of Fe(II)–PW_{11} into low-toxic species under neutral conditions. Besides, A-MIL-101@PW_{12} exhibited high cell lethality in HeLa cells based on the *in situ* synthesized Fe(II)–PW_{11} (Fig. 5e). Furthermore, live and dead cell staining experiments demonstrated the significant damage of HeLa cells treated by Fe(II)–PW_{11}, MIL-101@PW_{12} and A-MIL-101@PW_{12} groups (red signals represented cell death) (Fig. 5f). Therefore, Fe(II)–PW_{11} can achieve tumor-specific and efficient therapy through TME-activated *in situ* synthesis in cancer cells, which exhibits low toxicity to normal tissues upon postoperative degradation under neutral conditions.

Intracellular evaluation of ferroptosis induced by *in situ* synthesized Fe(II)–PW_{11}

The *in situ* synthesized Fe(II)–PW_{11} exhibits NOX-like and LOX-like activities to initiate ferroptosis at tumor sites. As illustrated (Fig. 6a), Fe(II)–PW_{11} facilitates LPO accumulation through PUFA-PL peroxidation and NADPH consumption. To confirm Fe(II)–PW_{11}-induced ferroptosis for cancer treatment, HeLa cells were incubated with different inhibitors of cell death, including the caspase inhibitor (Z-VAD-FMK and Boc-D-FMK),[38] necroptosis inhibitor (Nec-1),[39] ferroptosis inhibitor (Fer-1)[40] and ROS inhibitor (NAC).[41] As shown in Fig. 6b, significantly increased cell viability was recorded after treatment with the Fer-1 inhibitor, indicating that cell death was induced through ferroptosis, rather than apoptosis or necroptosis. In addition, cell viability was slightly restored after being treated with NAC, due to the recovery of GPX-4 activity for ferroptosis suppression.

First, the LPO accumulation induced by the *in situ* synthesized Fe(II)–PW_{11} was confirmed by the increased green fluorescence upon BODIPY 581/591 C11 oxidation in HeLa cells (Fig. 6c). Interestingly, this LPO accumulation is a ROS-independent process, demonstrated by the absence of ROS but significant LPO signals in cells after treating with A-MIL-101@PW_{12} for 12 h (Fig. S27†). while obvious ROS signals of $O_2^{\cdot-}$ were observed after 24 h (Fig. S28†) along with cell death, indicating the generation of ROS and $O_2^{\cdot-}$ upon stimulation of oxidative stress after cell death. Furthermore, with the ROS inhibitor NAC added, no significant ROS and $O_2^{\cdot-}$ (Fig. 6d) was observed but LPO accumulation was observed (Fig. S29†). This is in accordance with the ROS-independent LPO accumulation,

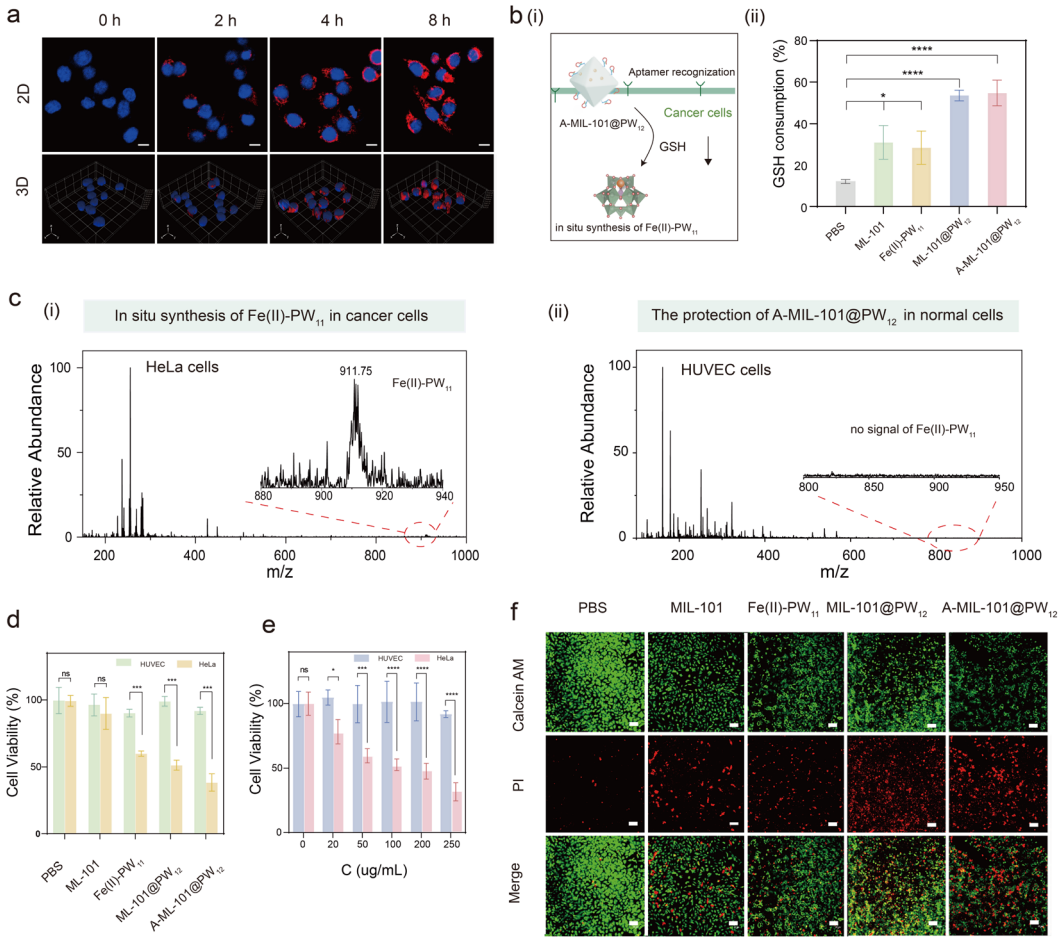

Fig. 5 Investigation on TME-induced *in situ* synthesis of Fe(II)–PW_{11} for cancer therapy. (a) Merged 2D and 3D Z-stack images of HeLa cells incubated with Cy5-A-MIL-101@PW_{12} for 0 h, 2 h, 4 h and 8 h. Red channel: Cy5-A-MIL-101@PW_{12}; blue channel: nuclei stained by Hoechst 33342. The scan bar is 10 μm. (b) The degradation of A-MIL-101@PW_{12} in HeLa cells. (i) The illustration of A-MIL-101@PW_{12} degradation and (ii) the GSH consumption after treatment with different groups. (c) The MS spectra of HeLa cell lysates (i) and HUVEC lysates (ii) after incubation with A-MIL-101@PW_{12}. (d) MTT assay of HeLa and HUVEC cells incubated with different groups. (e) MTT assay of HeLa cells incubated with different concentrations of A-MIL-101@PW_{12}. (f) CLSM images of HeLa cells and HUVECs with different treatments. The cells were stained with calcein-AM (green signals indicated living cells) and propidium iodide (PI) (red signals indicated cell death). The scan bar is 80 μm. Bars represent mean ± SD ($n = 3$ independent samples) calculated by the one-way ANOVA multiple comparison test (ns ($p > 0.05$), *$p < 0.05$, **$p < 0.01$, ***$p < 0.001$, and ****$p < 0.0001$).

exhibiting increased content of the LPO product (MDA) with or without the ROS inhibitor NAC added (Fig. 6e).

Additionally, the intracellular NADPH level in HeLa cells significantly decreased after treatment with Fe(II)–PW_{11}, MIL-101@PW_{12} and A-MIL-101@PW_{12} without (Fig. 6f) or with (Fig. S30†) the addition of NAC, indicating that *in situ* synthesized Fe(II)–PW_{11} facilitated the NADPH oxidation through the ROS-independent NOX/LOX cascade process. The decreased intracellular levels of BH_4 (Fig. 6g) and CoQ_{10} (Fig. 6h) in the A-MIL-101@PW_{12} group further confirm the inhibition of antioxidants regulated by NADPH. Furthermore, the decreased GPX4 and DHFR protein levels in the A-MIL-101@PW_{12} and Fe(II)–PW_{11} groups (Fig. 6i and S31–S33†) indicated the deactivation of GPX-4 and DHFR protein due to the decrease in GSH and BH_4 in HeLa cells.[42] Notably, the expression of the FSP1 protein remained unchanged, indicating that CoQ_{10} could have no effect on the activity of FSP1. Consequently, the *in situ* synthesized Fe(II)–PW_{11} can induce ferroptosis by reducing intracellular ferroptosis inhibitors and causing related protein deactivation.

Thereafter, intracellular Fe^{2+} content was also confirmed by the increased red fluorescence after treatment with A-MIL-101@PW_{12} (Fig. S34†). This demonstrated the promotion of the LIP by the generated $O_2^{\bullet-}$, which would promote the subsequent LPO process for the cancer therapy The efficient therapy has been confirmed by the distinct mitochondrial shrinkage and the increase in mitochondria membrane density in A-MIL-101@PW_{12}-treated HeLa cells (Fig. 6j).[43] Consequently, A-MIL-101@PW_{12} is effective for cancer therapy through ferroptosis induced by the *in situ* synthesized Fe(II)–PW_{11}.

In vivo evaluation of tumor suppression

To evaluate the *in vivo* therapeutic performance of the *in situ* synthesized Fe(II)–PW_{11}, HeLa-tumor-bearing mice were

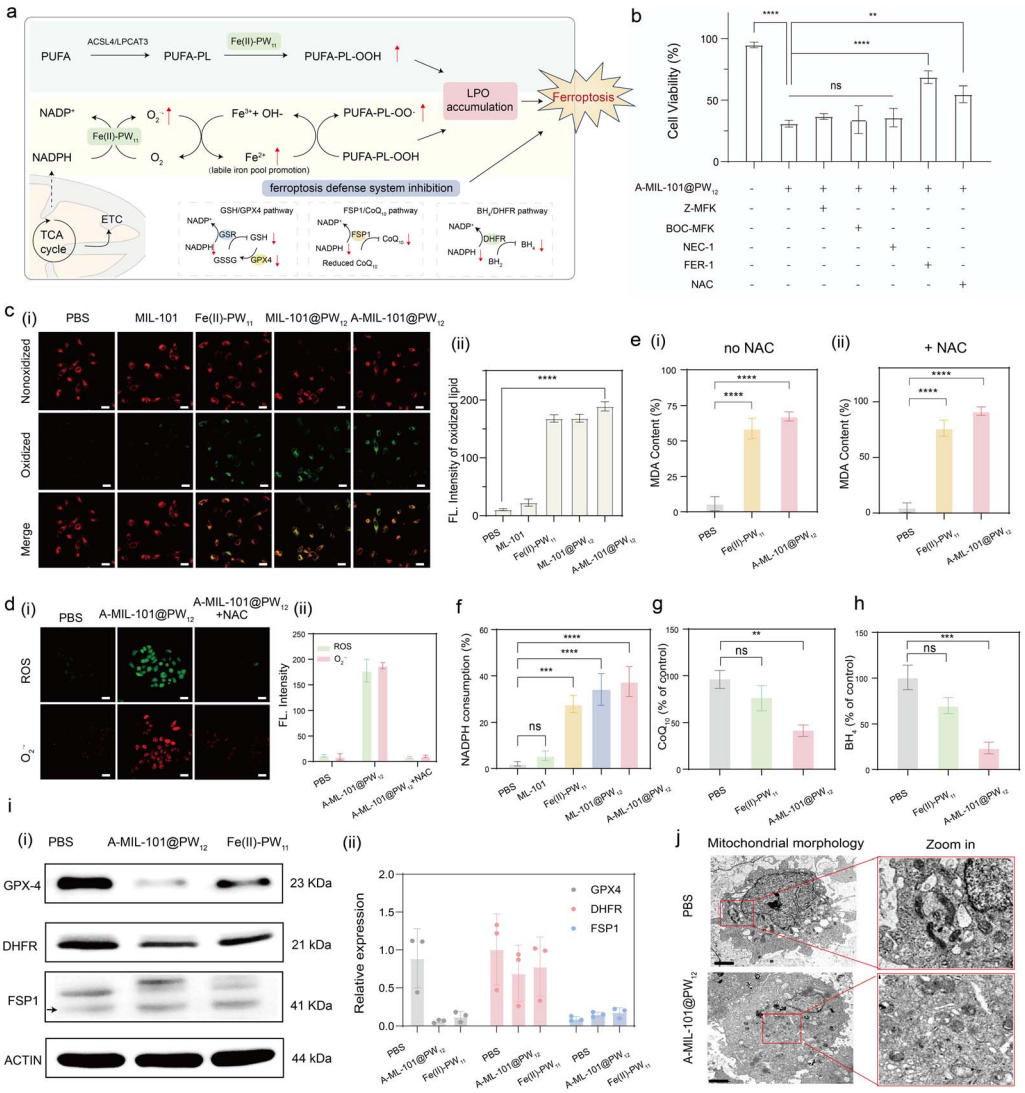

Fig. 6 Investigation of ferroptosis induced by *in situ* synthesized Fe(II)–PW_{11} in cancer cells. (a) Illustration of NADPH depletion and LPO accumulation for ferroptosis. (b) The cell viability of HeLa cells incubated with A-MIL-101@PW_{12} and different inhibitors. (c) The LPO verification in HeLa cells. (i) Cell imaging after treatment with different groups. (ii) The quantitative statistics of green fluorescence intensity of (i). The scan bar is 40 μm. (d) The ROS and $O_2^{\bullet-}$ generation. (i) The cell imaging treated with A-MIL-101@PW_{12} with NAC and without NAC. (ii) The quantitative statistics of fluorescence intensity of (i). The scan bar is 40 μm. (e) MDA content of HeLa cells (i) without NAC and (ii) with NAC after treatment with PBS, Fe(II)–PW_{11} and A-MIL-101@PW_{12}. (f) NADPH consumption, (g) CoQ_{10} content and (h) BH_4 content of HeLa cells after treatment with different groups. (i(i)) Western blotting assay of the GPX4, DHFR and FSP1 protein levels in cancer cells treated with PBS, Fe(II)–PW_{11} and A-MIL-101@PW_{12}. (ii) Quantitative analysis of GPX-4, DHFR and FSP1 protein expression based on the western blot data ($n = 3$). (j) The BioTEM image of HeLa cells treated with A-MIL-101@PW_{12}. The scar bar is 2 μm. Bars represent mean ± SD ($n = 3$ independent samples) calculated by the one-way ANOVA multiple comparison test (ns $p > 0.05$), *$p < 0.05$, **$p < 0.01$, ***$p < 0.001$, and ****$p < 0.0001$).

selected as models. Initially, for tracking the distribution of nanodrugs, fluorescent Cy5 was labeled on the AS1411 aptamer to prepare A-Cy5-MIL-101@PW_{12}. The HeLa-tumor-bearing mice were intravenously administered with A-Cy5-MIL-101@PW_{12} and the real-time fluorescence images were collected using an *in vivo* imaging system (IVIS) (Fig. S35†). As demonstrated, tumor sites showed stronger fluorescent signals, while normal tissues showed weaker ones. This was attributed to the enhanced permeability and retention effect of the nanocarrier as well as the tumor-targeting upon AS1411 recognition for *in vivo* therapeutic applications. Thereafter, the mice were subsequently sacrificed to obtain the main organs for *in vivo* imaging to identify the distribution of the nanomedicine. As demonstrated, A-Cy5-MIL-101@PW_{12} was mainly accumulated in tumor and liver tissue, demonstrating that nanocarriers in tumors would be excreted through metabolism after treatment.

Subsequently, the HeLa-tumor-bearing mice were injected with nanomedicines, which were randomly divided into five groups: saline (I), MIL-101 (II), Fe(II)–PW_{11} (III), MIL-101@PW_{12} (IV), and A-MIL-101@PW_{12} (V) (1.20 mg kg^{-1} with the reference LD_{50} studies) (Fig. 7a and S36†). These nanomedicines were injected into mice every 3 days and the tumor sizes and body

weights were monitored. Initially, the hemocompatibility assay of A-MIL-101@PW_{12} was confirmed by the low hemolysis rates and no significant heme release from the damaged erythrocytes (Fig. S37†). This indicated the negligible hemolytic toxicity, further confirmed by stable levels of biochemical indices in different groups (Fig. S38†).[44] Therefore, A-MIL-101@PW_{12} satisfied biosafety for the subsequent therapeutic applications. As monitored, the tumor growth was inhibited in the nanomedicine-treated groups compared with the control group (Fig. 7b). Specifically, the Fe(II)–PW_{11} group exhibited more efficient tumor inhibition than the MIL-101 groups and the most significant tumor suppression was observed in the A-MIL-101@PW_{12} group. The lowest tumor weight in the A-MIL-101@PW_{12} group also confirmed the efficient tumor treatment by *in situ* synthesized Fe(II)–PW_{11} (Fig. 7c). In addition, the tumor growth inhibition value (TGI) of the A-MIL-101@PW_{12} group was determined to be 60%, verifying the efficient therapy by the present strategy (Fig. 7d and e). The satisfactory therapeutic efficacy is not only attributed to NOX-like and LOX-like activities upon the cascade reaction but is also enhanced by GSH depletion. Meanwhile, no apparent change in body weight

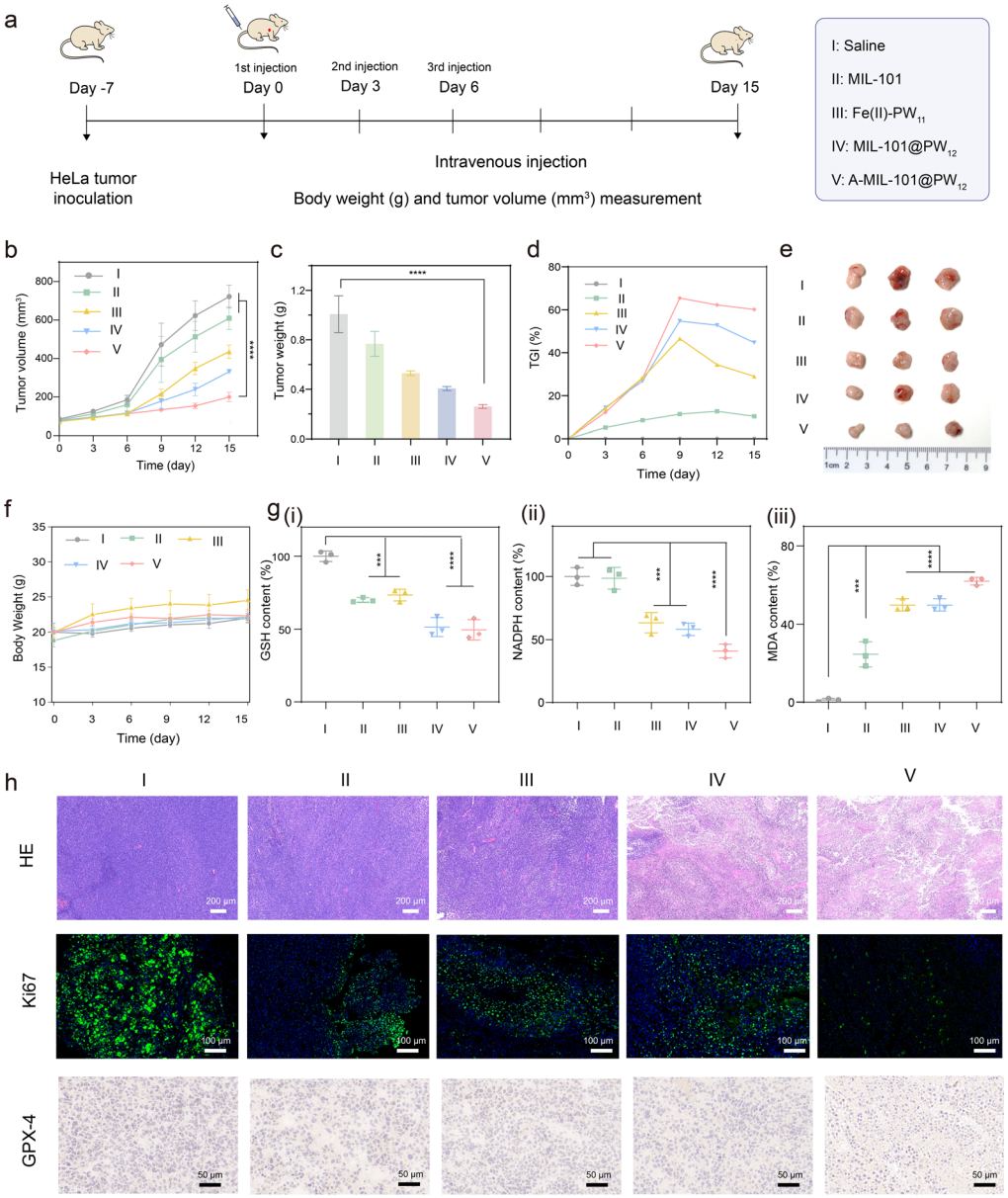

Fig. 7 *In vivo* therapeutic efficacy of the *in situ* synthesized Fe(II)–PW_{11}. (a) The illustration of a HeLa-bearing mice model for cancer therapy. Evaluation of tumor growth (b), tumor weight (c), and tumor growth inhibition ratio (d), and digital photos of excised tumors (e) and body weight (f) for different groups during the period of treatment. (g) The contents of GSH (i), NADPH (ii), and MDA (iii) in tumors after different treatments. (h) H&E, Ki67 and GPX4 images of the tissues from HeLa tumor-bearing mice after different treatments. (I) Saline; (II) MIL-101; (III) Fe(II)–PW_{11}; (IV) MIL-101@PW_{12}; (V) A-MIL-101@PW_{12}. Bars represent mean ± SD (n = 3 independent samples) calculated by the one-way ANOVA multiple comparison test (ns (p > 0.05), *p < 0.05, **p < 0.01, ***p < 0.001, and ****p < 0.0001).

indicated negligible side effects of these treatments on mice (Fig. 7f).

To evaluate the ferroptosis-induced cancer cell death, *in vivo* experiments at the tumor sites were conducted. As exhibited (Fig. 7g), the GSH levels in tumors decreased in the A-MIL101@PW_{12} treated groups, confirming the GSH-induced A-MIL101@PW_{12} degradation. Moreover, decreased NADPH and increased MDA were recorded in Fe(II)–PW_{11}, MIL-101@PW_{12} and A-MIL-101@PW_{12} groups, confirming NADPH depletion and LPO accumulation catalyzed by *in situ* synthesized Fe(II)–PW_{11}. Besides, the prominent downregulation of GPX4 in the A-MIL-101@PW_{12} group is in accordance with the ferroptosis-induced anticancer treatments (Fig. 7h). Therefore, the NADPH consumption and LPO accumulation were confirmed to induce ferroptosis for tumor-selective therapy.

Furthermore, the hematoxylin and eosin (H&E) staining assay was carried out to evaluate the antitumor activity, which exhibited significant damage to cancer cells (with a fragmentary cellular structure) in the A-MIL101@PW_{12} group. This confirmed the severe damage to tumors by the *in situ* synthesized Fe(II)–PW_{11} (Fig. 7h). In addition, the severe plasmatorrhexis and weakest cell proliferation were demonstrated by Ki67 staining of tumor slices after being treated with A-MIL-101@PW_{12}, while no obvious normal tissue necrosis was observed in H&E staining of major organs (heart, liver, spleen, lung, and kidney), indicating low toxicity to healthy tissues (Fig. S39†). This suggested that ferroptosis can be selectively initiated at tumor sites by the *in situ* synthesized Fe(II)–PW_{11}, which is postoperatively degraded into nontoxic debris in normal tissues. Therefore, upon the *in situ* synthesis of Fe(II)–PW_{11}, A-MIL-101@PW_{12} exhibited promising tumoricidal efficacy for cancer therapy with low side effects.

Conclusions

In conclusion, the enzymatic NOX-like and LOX-like activities, catalyzed by an *in situ* synthesized single-site catalyst (Fe(II)–PW_{11}), were reported for tumor-selective therapy *via* ferroptosis. The *in situ* synthesis of Fe(II)–PW_{11} was achieved by the chelation of Fe^{2+} into PW_{11} upon TME-activated degradation of iron-based nanocarriers in cancer cells. Upon electron transfer, Fe(II)–PW_{11} exhibits NOX-like activity for NADPH consumption and $O_2^{\bullet-}$ generation, which promotes the LIP to facilitate ferroptosis. Meanwhile, the formation of the high-valence Fe(IV)=O–PW_{11} intermediate subsequently catalyzes the generation of lipid hydroperoxide radicals through HAT based on LOX-like activity. Consequently, with cascade NOX–LOX activities, Fe(II)–PW_{11} promotes LPO accumulation for ferroptosis-based cancer therapy in a ROS-independent pathway. Besides, ferroptosis is further enhanced through the suppression of the antioxidant system by depleting GSH and NADPH. After treatment, Fe(II)–PW_{11} is degraded into low-toxic debris in the neutral environment of normal organs, reducing postoperative off-target toxicity. Furthermore, comprehensive characterization studies have supported the mechanism examination, facilitating the design of ferroptosis therapy upon cascade reactions. This strategy not only achieves selective and efficient ferroptosis therapy through a synergistic multi-enzymatic pathway in a ROS-independent pathway with minimized side effects, but also broadens the applications of single-site catalysts.

Ethical statement

All animal experimental protocols were reviewed and approved by the Animal Care and Use Committee of Institute of Beijing Normal University and complied with all relevant ethical regulations.

Data availability

The data supporting this article have been included as part of the ESI.†

Author contributions

X. Y. Ge and Y. Y. Yin conceived and designed the experiments for the project. X. Y. Ge, X. N. Wang and X. Li performed the characterization of the compounds. J. Ouyang carried out the data analysis. Y. Y. Yin performed the theoretical calculations. X. Y. Ge and N. Na prepared the initial manuscript, with all other authors contributing to revisions. N. Na supervised the project and acquired the funding. All authors discussed the results and provided feedback on the manuscript.

Conflicts of interest

There are no conflicts to declare.

Acknowledgements

We gratefully acknowledge the financial support provided by the National Natural Science Foundation of China (NNSFC, 22474010 and 22274012 to N. N.), the Fundamental Research Funds for the Central Universities (No. 2233300007 to N. N.), the National Key Research and Development Program of China (No. 2024YFA1509600 to N. N.) and the National Natural Science Foundation of China (NNSFC, 21675014 and 21974010 to J. O.).

Notes and references

1 S. J. Dixon, K. M. Lemberg, M. R. Lamprecht, R. Skouta, E. M. Zaitsev, C. E. Gleason, D. N. Patel, A. J. Bauer, A. M. Cantley, W. S. Yang, B. Morrison and B. R. Stockwell, *Cell*, 2012, **149**, 1060–1072.
2 G. Lei, L. Zhuang and B. Gan, *Nat. Rev. Cancer*, 2022, **22**, 381–396.
3 M. Conrad, S. M. Lorenz and B. Proneth, *Trends Mol. Med.*, 2021, **27**, 113–122.
4 Z. Liu, S. Liu, H. Jin, B. Liu, Q. Meng, M. Yuan, X. Ma, J. Wang, M. Wang, K. Li, P. Ma and J. Liu, *Angew. Chem., Int. Ed.*, 2024, e202414879.
5 X. Zhao, X. Wang, W. Zhang, T. Tian, J. Zhang, J. Wang, W. Wei, Z. Guo and X. Wang, *Angew. Chem., Int. Ed.*, 2024, **63**, e202400829.

6 R. Hu, X. Chen, Z. Li, G. Zhao, L. Ding, L. Chen, C. Dai, Y. Chen and B. Zhang, *Adv. Mater.*, 2023, **35**, 2306469.
7 Q. Yao, J. Fan, S. Long, X. Zhao, H. Li, J. Du, K. Shao and X. Peng, *Chem*, 2022, **8**, 197–209.
8 H. Zhang, Y. Chen, W. Hua, W. Gu, H. Zhuang, H. Li, X. Jiang, Y. Mao, Y. Liu, D. Jin and W. Bu, *Angew. Chem., Int. Ed.*, 2023, **62**, e202300356.
9 W. Xu, Y. Yang, L. Liu, B. Hu, Y. Tang, H. Ding, L. Zhang, P. Yang and C. Wang, *Adv. Funct. Mater.*, 2025, 2420540.
10 A. Seiler, M. Schneider, H. Förster, S. Roth, E. K. Wirth, C. Culmsee, N. Plesnila, E. Kremmer, O. Rådmark, W. Wurst, G. W. Bornkamm, U. Schweizer and M. Conrad, *Cell Metab.*, 2008, **8**, 237–248.
11 Y. Zou, H. Li, E. T. Graham, A. A. Deik, J. K. Eaton, W. Wang, G. Sandoval-Gomez, C. B. Clish, J. G. Doench and S. L. Schreiber, *Nat. Chem. Biol.*, 2020, **16**, 302–309.
12 A. Andreou and I. Feussner, *Phytochemistry*, 2009, **70**, 1504–1510.
13 X. Fang, H. Ardehali, J. Min and F. Wang, *Nat. Rev. Cardiol.*, 2022, **20**, 7–23.
14 T. M. Seibt, B. Proneth and M. Conrad, *Free Radical Biol. Med.*, 2019, **133**, 144–152.
15 K. Bersuker, J. M. Hendricks, Z. Li, L. Magtanong, B. Ford, P. H. Tang, M. A. Roberts, B. Tong, T. J. Maimone, R. Zoncu, M. C. Bassik, D. K. Nomura, S. J. Dixon and J. A. Olzmann, *Nature*, 2019, **575**, 688–692.
16 M. Soula, R. A. Weber, O. Zilka, H. Alwaseem, K. La, F. Yen, H. Molina, J. Garcia-Bermudez, D. A. Pratt and K. Birsoy, *Nat. Chem. Biol.*, 2020, **16**, 1351–1360.
17 B. Yang, H. Yao, J. Yang, C. Chen, Y. Guo, H. Fu and J. Shi, *J. Am. Chem. Soc.*, 2021, **144**, 314–330.
18 Y. Wang, S. Xu, L. Shi, C. Teh, G. Qi and B. Liu, *Angew. Chem., Int. Ed.*, 2021, **60**, 14945–14953.
19 J. Tian, B. Li, F. Zhang, Z. Yao, W. Song, Y. Tang, Y. Ping and B. Liu, *Angew. Chem., Int. Ed.*, 2023, **62**, e202307288.
20 Y. Liu, J. Zhang, X. Zhou, Y. Wang, S. Lei, G. Feng, D. Wang, P. Huang and J. Lin, *Angew. Chem., Int. Ed.*, 2024, **63**, e202408064.
21 Y. Yin, X. Ge, J. Ouyang and N. Na, *Nat. Commun.*, 2024, **15**, 2954.
22 H. Wang, T. Yang, J. Wang, Z. Zhou, Z. Pei and S. Zhao, *Chem*, 2024, **10**, 48–85.
23 J. Han and J. Gun, *Coord. Chem. Rev.*, 2023, **490**, 215209.
24 L. Zhao, Z. Li, J. Wei, Y. Xiao, Y. She, Q. Su, T. Zhao, J. Li and J. Shao, *Chem. Eng. J.*, 2022, **430**, 133057.
25 G. Liu, Y. Zhang, L. Xu, B. Xu and F. Li, *New J. Chem.*, 2019, **43**, 3469–3475.
26 C. Huang, C. Zhao, Q. Deng, H. Zhang, D. Yu, J. Ren and X. Qu, *Nat. Catal.*, 2023, **6**, 729–739.
27 C. Wu, D. Xu, M. Ge, J. Luo, L. Chen, Z. Chen, Y. You, Y. Zhu, H. Lin and J. Shi, *Nano Today*, 2022, **46**, 101574.
28 Y. Wang, M. Sun, J. Qiao, J. Ouyang and N. Na, *Chem. Sci.*, 2018, **9**, 594–599.
29 F. D. Hardcastle, *J. Raman Spectrosc.*, 1995, **26**, 397–405.
30 B. Viswanadham, N. Nagaraju, C. N. Rohitha, V. Vishwanathan and K. V. R. Chary, *Catal. Lett.*, 2018, **148**, 397–406.
31 W. Liao, H. Liu, L. Qi, S. Liang, Y. Luo, F. Liu, X. Wang, C. Chang, J. Zhang and L. Jiang, *Cell Rep. Phys. Sci.*, 2021, **2**, 100557.
32 M. Kamibayashi, S. Oowada, H. Kameda, T. Okada, O. Inanami, S. Ohta, T. Ozawa, K. Makino and Y. Kotake, *Free Radical Res.*, 2009, **40**, 1166–1172.
33 K. Teng, L. Ya and Q. Zheng, *J. Am. Chem. Soc.*, 2023, **145**, 4081–4087.
34 H. Huang, S. Banerjee, K. Qiu, P. Zhang, O. Blacque, T. Malcomson, M. J. Paterson, G. J. Clarkson, M. Staniforth, V. G. Stavros, G. Gasser, H. Chao and P. J. Sadler, *Nat. Chem.*, 2019, **11**, 1041–1048.
35 W. Kohn and L. J. Sham, *Phys. Rev.*, 1965, **140**, A1133–A1138.
36 T. Lu and F. Chen, *J. Comput. Chem.*, 2012, **33**, 580–592.
37 H. A. Shidy, *Dyes Pigm.*, 2017, **145**, 505–513.
38 H. Tu, W. Xiong, J. Zhang, X. Zhao and X. Lin, *Nat. Commun.*, 2022, **13**, 6603.
39 A. Degterev, Z. Huang, M. Boyce, Y. Li, P. Jagtap, N. Mizushima, G. Cuny, T. Mitchison, M. Moskowitz and J. Yuan, *Nat. Chem. Biol.*, 2005, **1**, 112–119.
40 R. Skouta, S. Dixon, J. Wang, D. Dunn, M. Orman, K. Shimada, P. Rosenberg, D. Lo, J. Weinberg, A. Linkermann and B. Stockwell, *J. Am. Chem. Soc.*, 2014, **26**, 4551–4556.
41 M. Halasi, M. Wang, T. Chavan, V. Gaponenko, N. Hay and A. Gartel, *Biochem. J.*, 2013, **454**, 201–208.
42 J. Zhang, H. Ge, D. Zhou, Q. Yao, S. Long, W. Sun, J. Fan, J. Du and X. Peng, *Adv. Mater.*, 2023, **35**, 2308205.
43 J. Cheng, L. Li, D. Jin, Y. Dai, Y. Zhu, J. Zou, M. Liu, W. Yu, J. Yu, Y. Sun, X. Chen and Y. Liu, *Adv. Mater.*, 2023, **35**, 2270037.
44 N. Song, R. Tao, H. Li, R. Zhang, Y. Huang, L. Zhang, Y. Liu, D. Yang and C. Yao, *Angew. Chem., Int. Ed.*, 2025, **64**, e202500566.